nature communications

Article

https://doi.org/10.1038/s41467-026-69198-2

Interfacial dipole engineering by self-assembled molecules in *n-i-p* and *p-i-n* perovskite solar cells

Received: 26 March 2025

Accepted: 27 January 2026

Published online: 04 February 2026

Check for updates

Mengde Zhai[1,2,3], Tianhao Wu[1,4], Kaihuai Du[5], Cheng Chen[2], Naoyuki Shibayama[6], Khongorzul Narmandakh[1,3], Abdul Haseeb Hassan Khan[7], Ying-Chiao Wang[7], Juan Shang[1], Aleksandar Staykov[1,4], Jun Tae Song[1], Shintaro Ida[4,8], Pangpang Wang[9], Sunao Yamada[9], Kaoru Tamada[10], Shuai Zhao[11,12], Aili Wang[5], Zhanglin Guo[1,3,4] ✉, Toshinori Matsushima[1,3,4] ✉, Tsutomu Miyasaka[6] & Ming Cheng[2] ✉

Self-assembled molecules are widely used as bottom interfacial layers in inverted perovskite solar cells, yet their application to perovskite top surfaces remains poorly understood. Here, we develop two self-assembled molecules for perovskite surface modification and interfacial optimization with the hole transport layer. Through solvent engineering, ordered and uniform molecular packing is achieved on the perovskite surface. These molecules optimize surface energetics and promote efficient hole transfer when coupled with a homologous hole transport layer. Their large molecular dipoles tune interfacial energy alignment and reduce energetic offsets, thereby accelerating charge extraction from the perovskite layer. This dipole-driven interfacial modulation is effective in both normal and inverted device architectures. As a result, a power conversion efficiency of 26.18% (certified 26.23%) is achieved in normal-structure devices, together with improved operational stability under maximum power point tracking. This work establishes a viable strategy for perovskite surface engineering using self-assembled molecules.

Perovskite solar cells (PSCs) are widely recognized as a promising next-generation photovoltaic technology and have achieved certified power conversion efficiency (PCE) exceeding 27%[1–5]. As PSCs consist of a multilayer stacked structure, interfacial heterojunctions play an increasingly critical role, particularly given that current technologies have significantly improved the bulk quality of perovskite (PSK) films[6–8]. Among these interfaces, the heterojunction between the perovskite and the hole transport layer (HTL) is a key factor influencing device performance, as perovskite surface defects and energy-level misalignment contribute to non-radiative recombination. This results in losses in open-circuit voltage (V_{OC}) and fill factor (FF), as well as long-term stability issue[9,10]. Introducing a rational passivation layer at this

[1]International Institute for Carbon-Neutral Energy Research (WPI-I2CNER), Kyushu University, Fukuoka, Japan. [2]Institute for Energy Research, School of Energy and Power Engineering, Jiangsu University, Zhenjiang, China. [3]Department of Automotive Science, Graduates School of Integrated Frontier Sciences, Kyushu University, Fukuoka, Japan. [4]Center for Energy Systems Design (CESD), International Institute for Carbon-Neutral Energy Research (WPI-I2CNER), Kyushu University, Fukuoka, Japan. [5]Institute of Technology for Carbon Neutralization, Yangzhou University, Yangzhou, Jiangsu, China. [6]Toin University of Yokohama, 1614 Kurogane-cho, Aoba, Yokohama, Kanagawa, Japan. [7]Department of Materials and Optoelectronic Science, National Sun Yat-sen University, Taiwan, China. [8]Institute of Industrial Nanomaterials (IINa), Kumamoto University, Kumamoto, Japan. [9]Materials Open Lab., Institute of Systems, Information Technologies and Nanotechnologies (ISIT), Fukuoka, Japan. [10]Institute for Materials Chemistry and Engineering, Kyushu University, Fukuoka, Japan. [11]College of Science, Chongqing University of Technology, Chongqing, China. [12]Chongqing Key Laboratory of New Energy Storage Materials and Devices, Chongqing University of Technology, Chongqing, China. ✉e-mail: guo.zhanglin.903@m.kyushu-u.ac.jp; tmatusim@i2cner.kyushu-u.ac.jp; mingcheng@ujs.edu.cn

interface is an effective strategy to suppress non-radiative recombination and enhance device stability[11,12]. For example, the organic halide salt phenylethylamine iodide (PEAI) is widely used to passivate perovskite surface defects and suppress non-radiative recombination[13]. Beyond defect passivation, surface-modifying molecules can also function as interfacial dipole modifiers, improving energy-level alignment[14,15]. For example, Miyasaka et al. demonstrated that phenethylamine halides (PEAX) generate interfacial dipoles at the perovskite/HTL interface, leading to a downward shift in the HTL energy level and an increase in V_{OC}[16]. Similarly, various interfacial molecules with combined passivation functions and tailored dipole moments have been successfully developed to optimize perovskite surface energetics and minimize interfacial charge accumulation[17–21]. Beyond passivation and dipole tuning, an ideal interfacial layer should also facilitate charge transfer by interacting with the HTL, for instance, by acting as a carrier channel to enhance charge selectivity and transport efficiency[22,23].

Self-assembled molecules (SAMs, note that the term "self-assembled monolayer" is not used here due to the difficulty of verifying true monolayer formation), such as Me-4PACz and MeO-2PACz, which feature a phosphonic acid anchoring group and a carbazole terminal group, are widely employed in high-efficiency *p-i-n* perovskite solar cells (PSCs)[24–31]. In these architectures, SAMs function as interface dipole modulators and can even serve as a single HTL[32]. This is attributed to the molecular asymmetry of SAMs, which results in electronic asymmetry, spatially separating positively and negatively charged groups and generating strong dipole moments[33–35]. These dipole moments facilitate energy-level alignment, while the terminal groups of SAMs act as efficient hole collectors due to their hole-selective properties[36–38]. Additionally, studies have shown that SAMs can strongly interact with perovskite, effectively reducing surface defects[39–42]. These characteristics make SAMs promising candidates for perovskite/HTL interfacial modification, enabling both surface passivation and efficient hole extraction. However, the application of SAMs for perovskite/HTL interface modification in *n-i-p* PSCs remains largely unexplored[43,44], and their functional roles in this configuration have yet to be thoroughly investigated. Furthermore, most reported SAMs exhibit relatively small dipole moments, and increasing the SAM layer thickness to enhance dipole accumulation often negatively impacts carrier transport. Therefore, developing suitable SAMs that can effectively modify the perovskite/HTL interface in *n-i-p* PSCs and elucidating their underlying mechanisms are critical yet challenging tasks.

Herein, we develop two SAMs, SFX-P1 and SFX-P2, with varying numbers of anchoring units to enhance the perovskite/HTL interface in *n-i-p* PSCs. Additionally, we employ a structurally similar material, SFX-DM, as HTL to establish layer-to-layer homogeneous hole transport (Fig. 1a). Our findings reveal that these SAM-modified perovskite surfaces effectively facilitate dipole tuning and enhanced hole extraction. The number of anchoring units plays a crucial role in

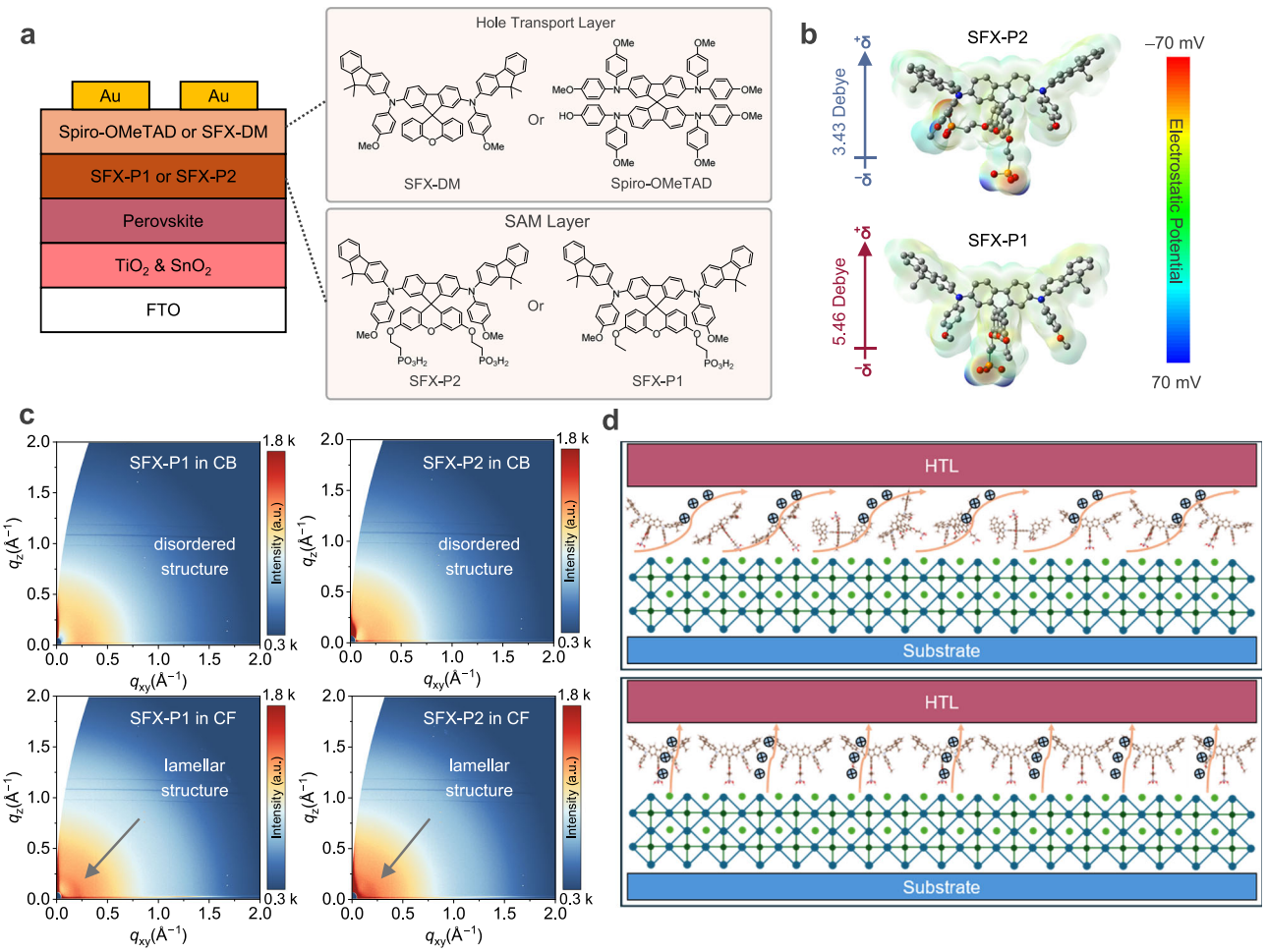

Fig. 1 | Fundamental properties and stacking behavior of SAM molecules. **a** Device architecture of the *n-i-p* perovskite solar cells. **b** ESP distributions and molecular dipole moments of SFX-P2 and SFX-P1 SAMs calculated by DFT. **c** 2D GIWAXS patterns of SFX-P1 and SFX-P2 films fabricated using CB or CF as the solvent. **d** Schematic illustration of the proposed molecular assembly behavior and hole transport characteristics of SAM layers fabricated with CB (first row) and CF (second row) solvents.

determining key properties such as solubility, dipole moment, and adsorption behavior on the perovskite surface, leading to distinct surface energetics between SFX-P1 and SFX-P2. Specifically, SFX-P1, which contains a single phosphonic acid group and an ethyl chain, exhibits more uniform adsorption on the perovskite surface due to its greater molecular flexibility compared to SFX-P2. The larger dipole moment of the SFX-P1-modified layer optimizes energy-level alignment at the perovskite/HTL interface, yielding a PCE of 26.18% in *n-i-p* PSCs. The encapsulated devices also show improved long-term operational stability under ambient humidity. Notably, the interfacial dipole tuning effect of these SAMs is also effective in *p-i-n* PSCs, demonstrating the universality of this strategy across different device configurations.

Results

Molecule properties

The synthetic routes and detailed procedures for both SAMs are illustrated in Supplementary Fig. 1. The terminal group with a spiro[fluorene-9,9′-xanthene] (SFX) core is synthesized via Buchwald-Hartwig coupling and cyclization reactions. Precise control of reactant equivalents and reaction time enables the selective synthesis of SFX-P2 and SFX-P1, each with different numbers of phosphonic acid anchoring groups. The chemical structures are confirmed by nuclear magnetic resonance (NMR) spectroscopy (^{1}H, ^{13}C, and ^{31}P) and matrix-assisted laser desorption ionization time-of-flight (MALDI-TOF) mass spectrometry (Supplementary Figs. 2-32). The electrostatic potential (ESP) distributions of both molecules are investigated using density functional theory (DFT) calculations (Fig. 1b). The results show that the negative ESP is primarily localized on the electron-rich phosphonic acid group, while the positive ESP is concentrated on the SFX core and donor units. Notably, SFX-P1 exhibits a larger dipole moment of 5.46 D, attributed to its greater electronegativity separation compared to SFX-P2 (3.43 D). This larger dipole moment enhances van der Waals interactions within the dipole array and the perovskite material, contributing to improved interfacial interactions[4,19,45].

Both SAMs exhibit high thermal stability, with decomposition temperatures (T_d) exceeding 210 °C (Supplementary Fig. 33). Additionally, SFX-P1 shows a glass transition temperature (T_g) of 133.8 °C, whereas no significant T_g is observed for SFX-P2, indicating their suitability for forming stable amorphous films[46,47]. The energy gap (E_g) and energy levels of both SAMs in solution are determined by cyclic voltammetry (CV) in combination with UV-vis absorption spectroscopy (Supplementary Fig. 34 and Supplementary Table 1), showing consistency with the energy-level trends obtained from DFT calculations (Supplementary Fig. 35). Furthermore, photoelectron yield spectroscopy (PYS) measurements reveal ionization potentials of −5.25 eV, −5.20 eV, and −5.10 eV for SFX-P2, SFX-P1, and SFX-DM films, respectively (Supplementary Fig. 36). These results suggest that the electron-withdrawing nature of the phosphonic acid group lowers the ionization potential of the molecules, making them well-suited as interfacial layers between perovskite and SFX-DM for optimized energy-level alignment.

When SFX-P2 and SFX-P1 function as interfacial layers, they can interact with the HTL through C-H···π bonding or electron density delocalization, influencing the hole transport distance[48–50]. To investigate this effect, we examined the intermolecular interaction energy (E_{int}) of SFX-P1 with Spiro-OMeTAD and SFX-DM using DFT calculations. As shown in Supplementary Fig. 37, the E_{int} of SFX-P1 with SFX-DM is −684 meV, significantly stronger than the −432 meV interaction energy observed for SFX-P1 with Spiro-OMeTAD. Additionally, the distance between the central sp^3-hybridized carbon atoms of SFX-P1 and SFX-DM is only 9.5 Å, which facilitates more efficient intermolecular hole transfer. These findings are consistent with the previous study[49], which demonstrated that a homologous interface layer/HTL design can enhance hole transport from the perovskite to the HTL.

Beyond the computational studies, the packing properties of organic molecules, such as crystallinity and orientation, which are influenced by solution treatment methods, are also crucial for their performance[51,52]. To investigate these properties, we examined the solubility and stacking characteristics of the two SAMs in chlorobenzene (CB) and chloroform (CF) solvents. As shown in Supplementary Fig. 38, SFX-P1 exhibits high solubility in both CB and CF (>5 mg mL^{-1}), whereas SFX-P2 shows lower solubility in both solvents. The enhanced solubility of SFX-P1 is likely due to its ethyl chain, which reduces molecular polarity and increases flexibility, thereby inhibiting molecular aggregation[46,53]. To further investigate the molecular stacking behavior, we performed grazing-incidence wide-angle X-ray scattering (GIWAXS) measurements on SAM films. Since ultra-thin SAM layers deposited on perovskite films do not produce detectable GIWAXS signals, we coated the SAMs onto silicon wafers for characterization. When CB is used as the solvent (Fig. 1c), both SFX-P2 and SFX-P1 films exhibit no significant diffraction signals, indicating their amorphous nature. Interestingly, when CF is used as the solvent (Fig. 1c), lamellar structures are observed in both SFX-P1 and SFX-P2 films, suggesting a more ordered molecular arrangement. This is further confirmed by broad peaks in the 1D GIWAXS profiles, indicative of π-π stacking interactions (Supplementary Fig. 39). Furthermore, analysis of the 1D GIWAXS profile confirms the presence of π-π stacking interactions with slip-stacking[54], as evidenced by a broad peak centered at approximately 1.35 Å^{-1}, corresponding to an interplanar distance of 4.65 Å. These findings suggest that when deposited on the perovskite surface using CF as a solvent, SAM molecules may form a more ordered arrangement through their anchoring units, although the interaction is not as strong as that observed on hydroxyl-rich metal oxide substrates[55]. The differences in SAM packing behavior when using CF (with units facing downward) versus CB (random arrangement) and the hole transport behaviors are illustrated schematically in Fig. 1d.

Photovoltaic performance

The above discussion on the properties of SAMs and their interactions with perovskite and HTL strongly suggests that the SAM interlayer influences the photovoltaic performance of PSCs. To investigate this effect, we fabricated *n-i-p* PSCs with the configuration shown in Fig. 1a. The optimal concentration of doped HTLs in PSCs was used to avoid the influence of HTL concentration on the SAM modification effect (Supplementary Figs. 40, 41). The reference device, based on SFX-DM as the HTL without SAM modification, is defined as the control. The *J-V* curve of the control device with champion performance is shown in Fig. 2a, exhibiting a PCE of 23.72%, a V_{OC} of 1.15 V, a short-circuit current density (J_{SC}) of 25.23 mA cm^{-2}, and an FF of 81.56%. Subsequently, we introduced the SAM modification layer, optimizing its concentration to 1 mg mL^{-1} in CF (optimization data in Supplementary Fig. 42 and Supplementary Tables 2, 3). Notably, the SAM layer not only enhances efficiency but also reduces hysteresis in the *J-V* curves. The device incorporating SFX-P2 spin-coated from CF (SFX-P2@CF) achieves a PCE of 25.65%, with a V_{OC} of 1.18 V, a J_{SC} of 25.73 mA cm^{-2}, and an FF of 84.51% (Fig. 2b). Meanwhile, the SFX-P1@CF-based device demonstrates an impressive PCE of 26.18% (certified 26.23%, Supplementary Fig. 43), with a V_{OC} of 1.19 V, a J_{SC} of 26.00 mA cm^{-2}, and an FF of 84.81% (Fig. 2c). The J_{SC} values are further confirmed by current density measurements from external quantum efficiency (EQE) spectra (Supplementary Fig. 44). Moreover, all three devices exhibit stable efficiency during stable power output tracking (Fig. 2d). We also achieve a high efficiency of 24.29% in a 1 cm^2 SFX-P1@CF device (Fig. 2e and Supplementary Table 4), together with improved reproducibility (Supplementary Fig. 45), demonstrating the scalability of SAM modification for fabricating high-performance large-area PSCs.

https://doi.org/10.1038/s41467-026-69198-2

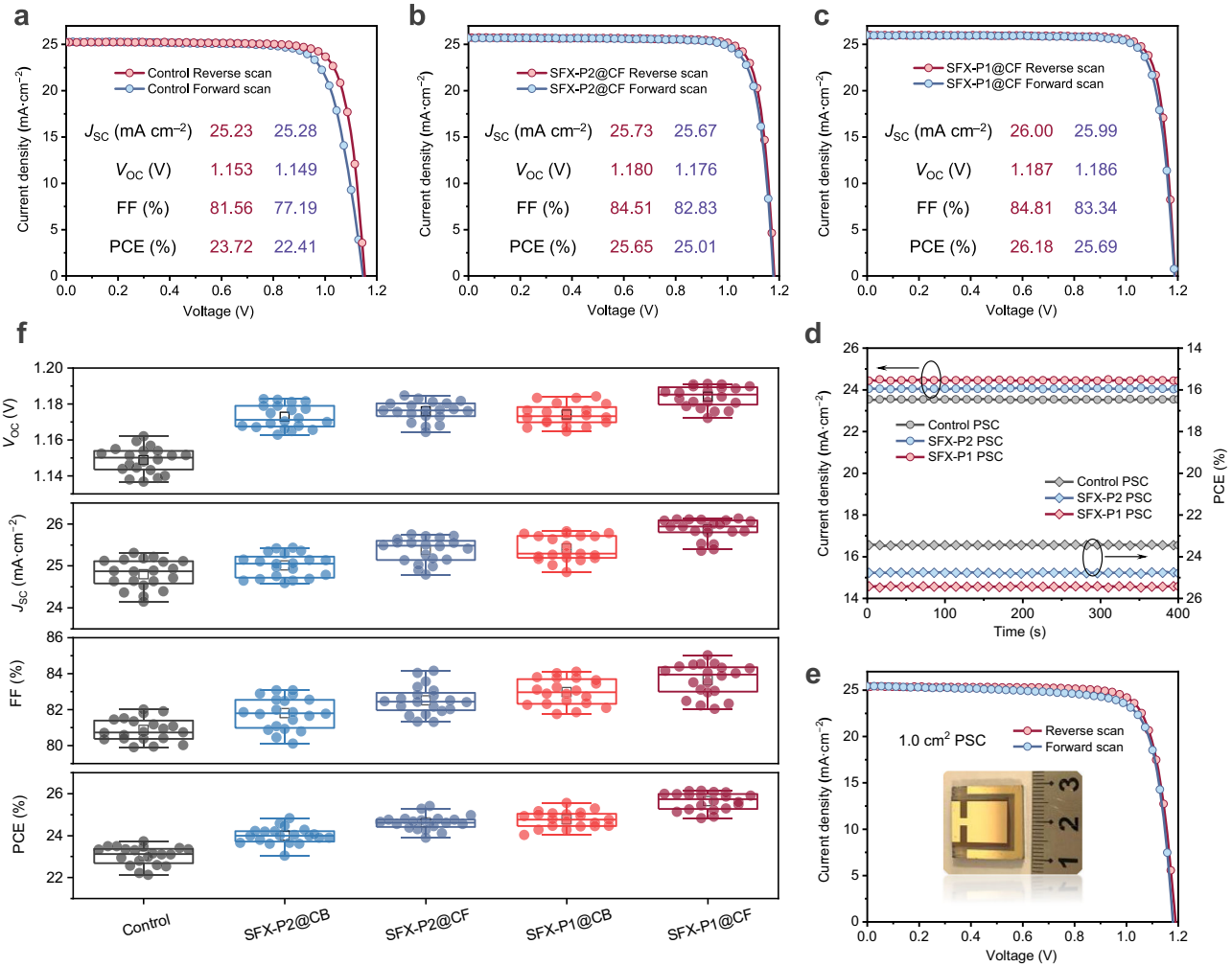

Fig. 2 | Photovoltaic performance. a *J-V* curves of champion PSCs using SFX-DM as HTL without SAM modifications. **b** *J-V* curves of champion PSCs using SFX-DM as HTL with SFX-P2 SAM modification. **c** *J-V* curves of champion PSCs using SFX-DM as HTL with SFX-P1 SAM modification. **d** Stabilized PCE and J_{SC} of champion PSCs using SFX-DM as HTL without and with SFX-P2 or SFX-P1 SAM modifications. **e** *J-V* curves of PSCs using SFX-DM as HTL with SFX-P1 SAM modification, with an active area of 1 cm^2. **f** Statistical photovoltaic parameters of PSCs using SFX-DM as HTL without and with SAM modifications. Sample size is 20. Whiskers limit the 1.5 interquartile range, the box identifies the 25th and 75th percentile and the horizontal line and the black empty square represent the median and mean values, respectively.

Additionally, SAM@CB devices also show enhanced performance (Supplementary Fig. 46), achieving a PCE of 25.67% for SFX-P1@CB. The CF-processed samples outperform their CB-processed counterparts, likely due to the more ordered molecular packing of SAMs when deposited from CF. This improved packing promotes stronger interactions between the SAM, perovskite, and HTL, thereby enhancing carrier transport and boosting efficiency. Figure 2f clearly illustrates the difference in device performance under different solvent processing conditions. Furthermore, when Spiro-OMeTAD is used as the HTL, we observe performance improvements upon SAM treatment (Supplementary Fig. 47). However, the champion efficiency of 25.13% achieved with SFX-P1@CF remains lower than that of its counterpart based on SFX-DM HTL. These results are consistent with our computational predictions and strongly support the conclusion that our homologous SAM design, with SFX-DM as the HTL, effectively enhances device performance.

Interfacial interactions

To understand the mechanisms by which SAM modification enhances *n-i-p* device performance, we investigated the packing properties of SAMs on the perovskite surface. In the following discussion, CF is used as the processing solvent for SAM deposition. We simulated the adsorption morphology of SFX-P1, SFX-P2, and SFX-DM on the $FAPbI_3$ perovskite surface and calculated the corresponding binding energy. As shown in Fig. 3a, the SFX-DM molecule adopts a parallel orientation on the perovskite surface, with a binding energy of only 33 meV due to the absence of anchoring groups (Supplementary Fig. 48), indicating negligible interaction between SFX-DM and the perovskite surface. In contrast, SAMs containing phosphonic acid anchoring groups exhibit strong charge redistribution upon adsorption onto the perovskite surface (Fig. 3b, c). The binding energy values for the SFX-P2 and SFX-P1 systems are −801 meV and −424 meV, respectively, suggesting that SAMs preferentially adsorb and interact with the perovskite surface via their anchoring groups. Furthermore, the adsorption morphology of SFX-P1 closely resembles that of SFX-DM, which may enhance the connectivity between the SAM layer and the HTL. We also conducted solvent rinse tests using CB (solvent for HTL). Energy-dispersive X-ray spectroscopy (EDS) elemental analysis reveals negligible reduction in phosphorus elemental mapping intensity (Supplementary Fig. 49), and photoluminescence (PL) intensity shows only a slight decrease after CB

https://doi.org/10.1038/s41467-026-69198-2

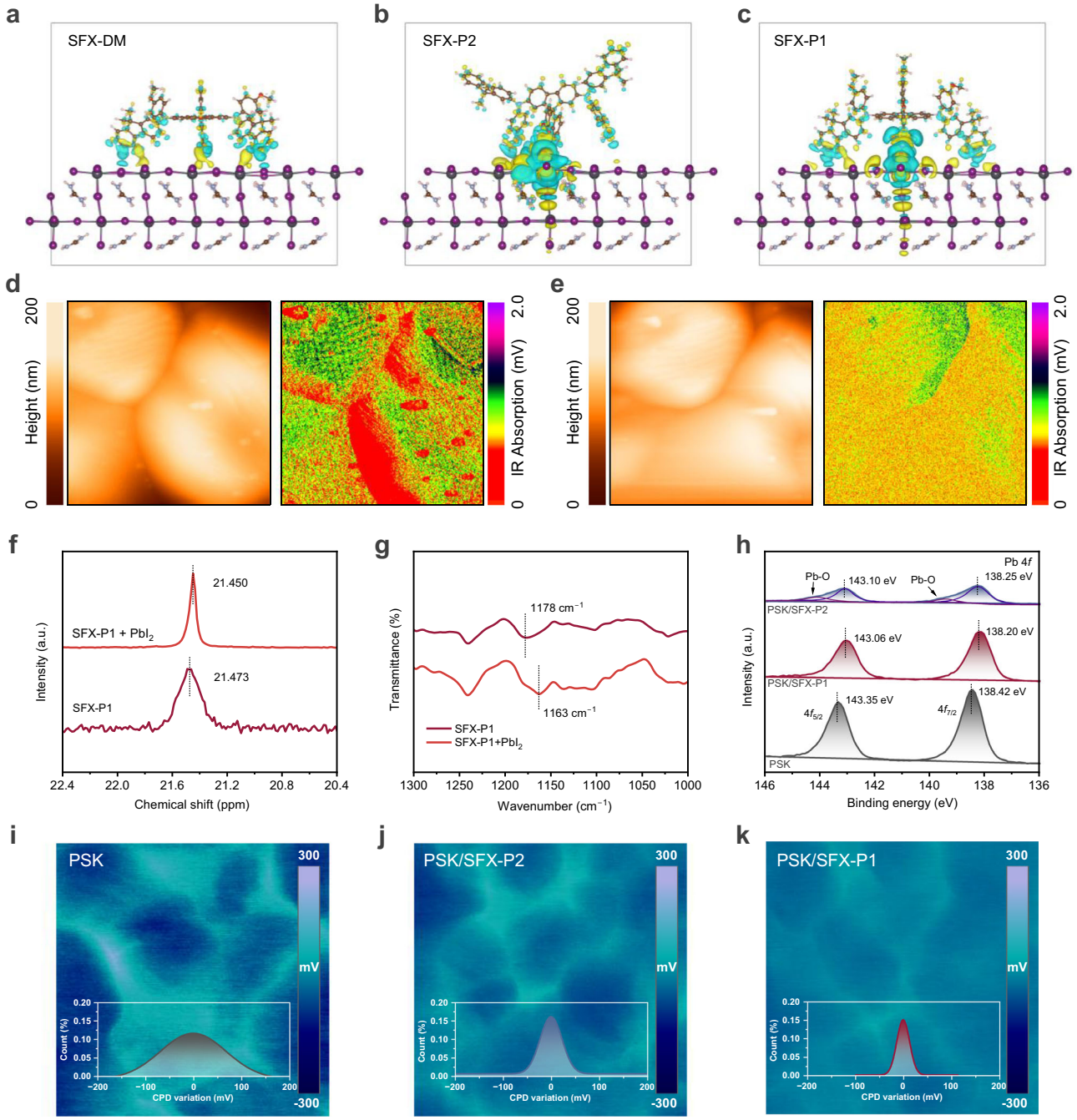

Fig. 3 | Interactions and film characterization. a DFT simulation of the adsorption models of a SFX-DM, **b** SFX-P2, and **c** SFX-P1 molecules on the perovskite surface, along with charge redistribution plots (positive charge in yellow, negative charge in turquoise) illustrating molecular interactions. AFM topography images (left) and local infrared (IR) absorption mapping profiles at 1462 cm^{-1} (right) of perovskite films coated with **d** SFX-P2 and **e** SFX-P1. The dimension of the scanning area in AFM images is 2 μm by 2 μm. **f** ^{31}P-NMR spectrum and **g** FTIR spectra of SFX-P1 before and after interaction with PbI_2. **h** XPS spectra of Pb peaks for the perovskite films without and with SFX-P2 or SFX-P1 SAM modification. KPFM images of **i** pristine perovskite film, **j** perovskite/SFX-P2 film, and **k** perovskite/SFX-P1 film. Insets show the CPD distributions derived from surface potential images. The dimension of the scanning area in KPFM images is 6 μm by 6 μm.

washing (Supplementary Fig. 50). This confirms that the SAM layer remains intact on the perovskite surface and is not affected by the HTL deposition process.

To further analyze the nanoscale molecular distribution on the perovskite surface, we employed atomic force microscopy coupled with infrared spectroscopy (AFM-IR), an ultra-high-resolution chemical analysis technique that detects molecular distributions by identifying IR responses at specific wavenumbers through AFM cantilever force signals[39,48,56]. The P-C stretching vibration located at 1,462 cm^{-1} was selected as the characteristic IR signal (Supplementary Fig. 51). As shown in Fig. 3d, the IR absorption intensity at grain boundaries in SFX-P2-coated perovskite films is lower than that at the surface, with numerous regions exhibiting weak IR absorption. This suggests poor and non-uniform adsorption of the SFX-P2 SAM on the perovskite surface. In contrast, SFX-P1-coated perovskite films exhibit a much more uniform IR absorption intensity (Fig. 3e), indicating uniform adsorption of SFX-P1 on the perovskite surface. The superior stacking uniformity of SFX-P1 can be attributed to the presence of ethyl chains,

which reduce molecular self-aggregation and promote a more uniform molecular distribution.

To further understand how SAM modification influences perovskite morphology and crystallinity, we performed scanning electron microscopy (SEM) and atomic force microscopy (AFM) imaging. The results show that SAM treatment reduces the presence of secondary grains in pristine perovskite films, leading to smoother and more uniform surfaces (Supplementary Figs. 52, 53). Additionally, X-ray diffraction (XRD) patterns reveal a decrease in the full width at half maximum (FWHM) of SAM-modified perovskite films (Supplementary Fig. 54 and Supplementary Table 5), indicating improved crystallinity. This observation is further supported by the increased intensity of the (001) and (002) crystal planes in 2D GIWAXS images and their corresponding 1D profiles (Supplementary Figs. 55, 56, and Supplementary Table 6). Notably, all films exhibit identical absorption spectra (Supplementary Fig. 57), confirming that SAM modification primarily enhances interfacial quality rather than altering bulk optical properties. These results suggest that SAM treatment improves perovskite surface quality, thereby facilitating hole transport at the interface.

To investigate the chemical interactions between SAMs and the perovskite surface, we performed ^{31}P NMR spectroscopy. The electron cloud density of phosphorus in the SAM increased, causing an up-field shift in the chemical signal after PbI_2 addition (Fig. 3f and Supplementary Fig. 58), which can be attributed to P = O coordination with Pb^{2+}[57]. FTIR further supports this interaction, as the P = O stretching vibrations of SFX-P1 and SFX-P2 shift from 1,178 cm^{-1} to 1,163 cm^{-1} and 1,173 cm^{-1}, respectively, upon PbI_2 addition (Fig. 3g and Supplementary Fig. 59), confirming coordination between P = O and Pb^{2+}. X-ray photoelectron spectroscopy (XPS) analysis further verifies these interactions. The Pb 4*f* characteristic peaks in pristine perovskite films shift to lower binding energies after SAM modification (Fig. 3h), indicating an increase in the electron cloud density around Pb atoms[58]. Additionally, the P 2*p* peak in the SAMs shifts toward higher binding energy (Supplementary Fig. 60). In the perovskite/SFX-P2 film, stronger ionic Pb-O bonding signals arising from the interaction between Pb^{2+} and -P-O$^-$ ions are observed at 138.25 eV and 143.10 eV, which leads to the shift of the Pb peaks toward higher binding energies[59,60]. The difference in XPS curves between SFX-P1 and SFX-P2 can be attributed to the stronger anchoring effect of SFX-P2, enabled by its double phosphoric acid groups. This result is consistent with the calculated binding energy values. The I 3*d* peaks also shift (Supplementary Fig. 61), indicating a change in the [PbI_6] electron cloud density. Kelvin probe force microscopy (KPFM) was performed to investigate the surface energetics of perovskite films by scanning surface potential fluctuations. As shown in Fig. 3i–k, the SFX-P1 SAM-modified perovskite surface exhibits the narrowest contact potential difference (CPD) distribution (~80 mV over a 4 × 4 μm^2 area), compared to 160 mV for SFX-P2 SAM-modified films and 300 mV for pristine perovskite films. These CPD distributions are consistent with the AFM-IR results, indicating that the uniform molecular packing of SFX-P1 minimizes potential fluctuations. These findings confirm that SAM treatment effectively balances the surface energetics of perovskite films, thereby improving carrier extraction[61,62]. In summary, our results confirm that SAMs, particularly the SFX-P1 interfacial layer, form strong interactions with both the perovskite and HTL, enhancing hole transport and ultimately improving solar cell performance.

Carrier dynamics

To further investigate the impact of the SAM layer on carrier dynamics at the perovskite/HTL interface in *n-i-p* PSCs, we examined its influence on interfacial energy alignment. As discussed earlier, the large dipole moment of SAMs is expected to affect carrier transfer at the interface. Therefore, we analyzed the energy-level alignment properties using ultraviolet photoelectron spectroscopy (UPS) (Supplementary Fig. 62), and the detailed schematic of the energy-level arrangement is depicted in Fig. 4a. Specifically, the work function (WF) of bare perovskite decreases from 4.67 eV to 4.52 eV and 4.38 eV after surface treatment with SFX-P2 and SFX-P1, respectively. This reduction in WF is attributed to the negative dipole formed by the SAM at the perovskite/HTL interface[17,44], which induces a downward shift in the local vacuum level. The valence band maxima (VBM) of bare perovskite, perovskite/SFX-P2, and perovskite/SFX-P1 films are determined to be −5.59 eV, −5.55 eV, and −5.48 eV, respectively, consistent with our PYS measurements (Supplementary Fig. 63). Given the constant bandgap (E_g) of 1.54 eV, the conduction band minima (CBM) are calculated as −4.05 eV, −4.01 eV, and −3.94 eV, respectively. Typically, the energy-level offset between the VBM of perovskite and the highest occupied molecular orbital (HOMO) of the HTL plays a crucial role in the efficient separation of photogenerated hole carriers. Since the exciton binding energy of perovskite materials is relatively low (20–73 meV), minimizing this energy offset is critical for reducing non-radiative exciton recombination in the active layer[16]. As shown in Fig. 4a, the SFX-P1-treated perovskite film exhibits a remarkably low energy-level offset of 90 meV, compared to 300 meV for SFX-P2 and 490 meV for the control sample. Additionally, SFX-P1 modification increases the energy gap between the CBM of perovskite and the HOMO of the HTL to 1.45 eV, which is expected to enhance the V_{OC} by reducing carrier recombination[63].

To evaluate the effect of SAMs on interfacial carrier transport, we developed a SCAPS-1D drift-diffusion (DD) model to simulate the band alignment and carrier diffusion behavior in different device configurations (Supplementary Fig. 64 and Supplementary Tables 7–9). The conduction band offset (CBO) and valence band offset (VBO) are calculated using the standard band alignment equations:

$$\mathrm{CBO} = \chi_{BaHfS_3} - \chi_{HTL} \tag{1}$$

$$\mathrm{VBO} = \chi_{HTL} + E_{g_{HTL}} - (\chi_{BaHfS_3} + E_{g_{BaHfS_3}}) \tag{2}$$

In the control configuration, where SFX-DM is directly used as the HTL without any interfacial layer, the VBO at the perovskite/HTL interface is −0.338 eV, forming a small valence band cliff (Supplementary Fig. 65a and Supplementary Table 10). Such a small cliff can facilitate hole extraction by providing a gentle driving force. The large CBO of +1.7 eV at the HTL/perovskite interface helps suppress electron leakage into HTL, thereby reducing interfacial recombination. Introducing a buffer layer (SFX-P1) between the perovskite and SFX-DM further optimizes the interface. As shown in Supplementary Fig. 65b and Supplementary Table 10, the VBO at the perovskite/SFX-P1 interface remains −0.34 eV, while a slight positive VBO of +0.02 eV appears at the SFX-P1/SFX-DM junction. This small valence-band spike increases the built-in potential (V_{bi}) across the interface, suppresses hole back-injection, and reduces interfacial recombination, while maintaining efficient hole extraction (spikes > 0.3 eV would instead hinder transport). In addition, we exclude the influence of the SFX-P1 buffer-layer doping concentration on device performance (Supplementary Fig. 66 and Supplementary Tables 11, 12), indicating that interfacial band alignment is the key factor governing efficiency enhancement.

The recombination-generation profile (Supplementary Fig. 67) confirms that the SFX-P1-modified device exhibits a lower recombination rate compared with the control configuration. Solving the coupled semiconductor equations within the DD framework also predicts clear improvements in V_{OC} and PCE for devices incorporating the SFX-P1 interfacial layer (Supplementary Table 13). These results confirm that the SFX-P1 layer not only optimizes energetic alignment but also suppresses recombination, enabling more efficient charge extraction and improved overall device performance.

Furthermore, improved band alignment enhances recombination resistance in SAM-modified actual PSCs (Supplementary Fig. 68), while

https://doi.org/10.1038/s41467-026-69198-2

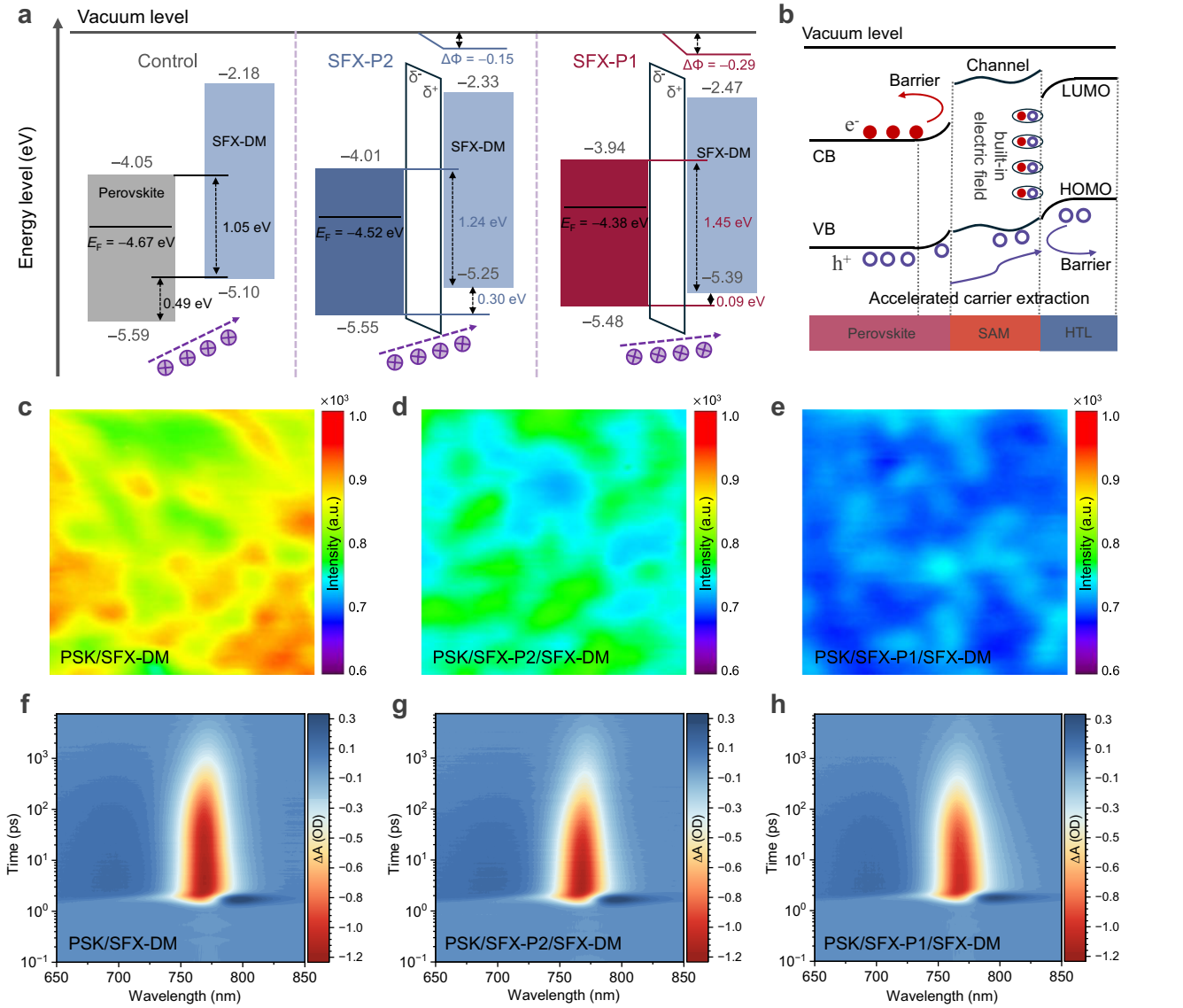

Fig. 4 | Energy level alignment and carrier dynamics. a Schematic band diagram illustrating the energy-level alignment at perovskite/HTL interface without and with SAM interfacial dipoles. **b** Schematic representation of the field effect induced by SAM-mediated energy-level modulation. PL intensity mapping images of **c** perovskite/SFX-DM film, **d** perovskite/SFX-P2/SFX-DM film, and **e** perovskite/SFX-P1/SFX-DM film. The dimension of the scanning area in PL intensity mapping images is 5 μm by 5 μm. Pseudocolor fs-TAS plot of **f** perovskite/SFX-DM, **g** perovskite/SFX-P2/SFX-DM, and **h** perovskite/SFX-P1/SFX-DM samples pumped at 2.41 eV.

suppressing interfacial charge accumulation and leading to a rise in V_{bi} (Supplementary Fig. 69). Although Mott-Schottky analysis may not yield fully quantitative values under the present conditions, the observed trends are consistent with both the DD simulations and other experimental findings, supporting the proposed mechanism. Overall, as illustrated in Fig. 4b, SAMs induce energy-level realignment via dipole arrays, where the phosphonic acid unit anchors to the perovskite surface, generating interfacial polarization that enhances the V_{bi}. These effects accelerate hole extraction and separation while suppressing carrier recombination at the interface, ultimately improving solar cell performance.

The PL and TRPL measurements (Supplementary Fig. 70) reveal that both the PL intensity and lifetime of SAM- and SAM/SFX-DM-coated samples are reduced, which may result from either increased non-radiative recombination or enhanced hole extraction at the interface. However, considering the improved device performance and structural characterizations, degradation of the perovskite film is unlikely. In the pristine perovskite samples, the τ_1 component associated with defect-assisted non-radiative recombination at interfaces or grain boundaries is relatively minor (Supplementary Table 14), while the τ_2 component from intrinsic luminescence dominates. After organic-layer deposition, τ_1 becomes shorter and its relative amplitude increases, supporting the occurrence of hole extraction. The τ_2 component also decreases due to efficient charge transfer. Transient photocurrent (TPC) and transient photovoltage (TPV) measurements (Supplementary Fig. 71) further confirm faster charge extraction (τ_{TPC} = 0.60 μs vs. 0.87 μs) and longer recombination lifetimes (τ_{TPV} = 4.56 μs vs. 3.60 μs) in SFX-P1-modified devices, evidencing improved interfacial charge transfer and suppressed trap-induced recombination. More importantly, the enhanced hole extraction exhibits a highly uniform distribution in PL mapping images (Fig. 4c–e), which is attributed to the uniform anchoring of SFX-P1 on the perovskite surface, as confirmed by AFM-IR.

The femtosecond transient absorption (fs-TA) spectroscopy was employed to further investigate carrier kinetics. The pseudo-color TA plots of the samples (Fig. 4f–h) display prominent ground-state

bleaching at ≈769 nm, where bleaching intensity reflects the number of carriers in the conduction and valence bands of the perovskite[64]. The trend in bleaching intensity follows: perovskite/SFX-P1/SFX-DM <perovskite/SFX-P2/SFX-DM <perovskite/SFX-DM, indicating that the SFX-P1-modified perovskite/HTL interface is the most favorable for hole transport. This trend is consistent with the faster decay of the perovskite/SFX-P1/SFX-DM sample over time (Supplementary Fig. 72). The photo-bleaching decay curves are fitted to further analyze charge dynamics using a tri-exponential function (Supplementary Fig. 73), with the extracted decay parameters summarized in Supplementary Table 15. The shortest lifetime component (τ_1) corresponds to hole trapping at the perovskite/HTL interface[65]. Compared to perovskite/SFX-DM samples, the incorporation of SFX-P2 and SFX-P1 SAMs reduces τ_1 from 201.3 ps to 128.2 ps and 109.5 ps, respectively, indicating ultrafast trap filling and carrier injection, thereby enhancing V_{OC}. Additionally, a significant reduction in the second lifetime component (τ_2), associated with hole extraction from perovskite to HTL, is observed for SAM-modified samples[66]. This effect is attributed to optimized energy-level alignment via the SAM-induced dipole effect, facilitating efficient exciton separation and resulting in higher FF. The longest lifetime component (τ_3), assigned to carrier lifetime, is longer in samples containing SAM, indicating suppressed carrier recombination. In summary, SAM modification, particularly with SFX-P1, not only passivates the perovskite surface but also accelerates hole extraction from the perovskite to the HTL through its dipole-induced energy-level tuning effect at the perovskite/HTL interface. The above results and discussion indicate that molecular adsorption behavior and interfacial energy-level modulation are the dominant factors affecting the performance of SFX-P2- and SFX-P1-based devices.

To validate our conclusions and assess the universality of our strategy, we also apply SAMs to modify the perovskite/ NiO_x HTL interface in *p-i-n* PSCs. We fabricated *p-i-n* devices with the structure ITO/NiO_x/SAM/perovskite/C60/BCP/Ag and evaluated their photovoltaic performance (Supplementary Fig. 74). The corresponding EQE spectra (Supplementary Fig. 75) indicate that the SAM layer has a negligible effect on light absorption in the 300–450 nm range, which can be attributed to its minimal parasitic absorption. Compared with the control *p-i-n* PSCs, which exhibit a PCE of 22.71% (reverse scan) and 22.22% (forward scan), the device incorporating the SFX-P1 SAM achieves a higher performance of 24.10% (reverse scan) and 23.93% (forward scan), along with reduced hysteresis. The SFX-P2 SAM also enhances device performance, though less effectively than SFX-P1, consistent with previous discussions. These results confirm that SAMs can universally enhance photovoltaic performance in inverted PSCs, demonstrating their effectiveness across different device configurations. In the *p-i-n* architecture, SAMs anchor directly onto the NiO_x surface, and the homologous interaction between the SAM and HTL, as discussed in the *n-i-p* structure, is absent. Consequently, dipole-moment modulation and enhanced hole extraction become the primary mechanisms driving performance improvement. To verify this, we employed UPS to investigate the band alignment at the buried interface. As shown in Supplementary Figs. 76–78, the SAM with negative dipole orientation at the buried interface reduces the work function of the NiO_x layer and simultaneously induces a downward shift in the perovskite Fermi level. The resulting energy-level alignment, characterized by a reduced interfacial energy barrier, facilitates more efficient separation and transport of photo-generated holes at the perovskite bottom interface. Therefore, in *p-i-n* PSCs, our SAMs also effectively regulate interfacial energy alignment and enhance hole extraction.

Long-term durability

Finally, we evaluated the durability of *n-i-p* PSCs under various conditions. Compared to the bare perovskite film, SAM-treated perovskite films exhibit an increased water contact angle (Supplementary Fig. 79), indicating improved resistance to moisture ingress. XRD analysis further confirms this protective effect (Supplementary Fig. 80); after 240 hours of exposure to ambient air with 60% humidity, the pristine perovskite film fully degrades into the non-photoactive yellow phase, whereas the SAM-modified perovskite films retain their black-phase stability. Similarly, when unencapsulated devices are stored in humid air (30–40% humidity), PSCs incorporating SFX-P2 and SFX-P1 retain 83% and 90% of the initial PCE, respectively, after 2500 hours, whereas the control PSCs remained only 34% (Fig. 5a). Additionally, thermal stability tests were conducted at 85 °C in an N_2 atmosphere (Fig. 5b). After 500 hours of aging, the unencapsulated SFX-P1 device maintains 87% of its initial efficiency, outperforming the SFX-P2-based (80%) and the control ones (35%).

To elucidate the role of the SAM layer in enhancing the solar cell durability, we compared fresh devices with those aged for 100 hours under 30-40% humidity at 85 °C. Cross-sectional SEM images of the devices before and after aging (Supplementary Fig. 81) reveal that perovskite degradation, specifically collapse at the perovskite/HTL interface, is observed only in the control sample, likely due to moisture infiltration. To further investigate the degradation mechanisms, we employed time-of-flight secondary ion mass spectrometry (TOF-SIMS) to analyze ion migration. As shown in Fig. 5c and 5e, during the aging process, Li^+ ions from the HTL migrate toward the SnO_2 ETL, consistent with previous reports[67]. This migration accelerates perovskite decomposition and phase transition in the presence of moisture[68,69]. Additionally, Li^+ diffusion from the HTL into the perovskite reduces the conductivity of the HTL, leading to performance degradation under prolonged high-temperature conditions[69]. Encouragingly, Li^+ ion migration is suppressed in devices incorporating the SFX-P1 layer, as indicated by the nearly unchanged Li^+ ion distribution in fresh and aged samples (Fig. 5d and 5f). These findings confirm that SAMs not only mitigate moisture infiltration due to their hydrophobic properties but also effectively block Li^+ ion migration across the device, thereby enhancing both moisture and thermal stability.

We then evaluated the operational stability of the devices. Under an N_2 atmosphere without encapsulation, the control and SFX-P1 PSCs retain 71.5% and 95.2% of their initial efficiencies, respectively, after 1000 hours of MPP tracking (Supplementary Fig. 82). More importantly, under real environmental conditions (30–40% humidity) following the ISOS-L-2 protocol, encapsulated SFX-P1 PSC retains 89.6% of its initial efficiency after 1300 hours of MPP tracking (Fig. 5g), with a projected T_{80} lifetime of 2800 hours based on linear extrapolation, far exceeding that of the control devices. Even under severe high-temperature conditions with continuous light illumination (Supplementary Fig. 83), the SFX-P1 PSCs maintain stable output due to enhanced interfacial quality and suppressed ion migration, in contrast to the control devices, which exhibit pronounced fluctuations during operation.

Discussion

We develop a strategy for modifying the perovskite/HTL interface using SAMs. The SAMs, particularly SFX-P1, exhibit strong and ordered molecular packing on the perovskite surface (achieved through solvent engineering), which effectively minimizes surface defects and enhances hole transfer to the homologous SFX-DM HTL. The dipole-induced energy-level modulation minimizes the interfacial energy offset to 90 meV, accelerating hole extraction and transfer. The uniform and densely packed SFX-P1 layer further improves carrier dynamics, resulting in a remarkable PCE of 26.18% (certified 26.23%) in *n-i-p* PSCs, along with enhanced long-term durability. Notably, encapsulated devices retain 89.6% of their initial efficiency after 1300 hours of MPP tracking under real-world conditions, with a projected T_{80} lifetime of 2800 hours. Furthermore, this SAM interfacial modification is also effective in *p-i-n* PSCs, confirming its universality across different device architectures. This study introduces SAMs for

https://doi.org/10.1038/s41467-026-69198-2

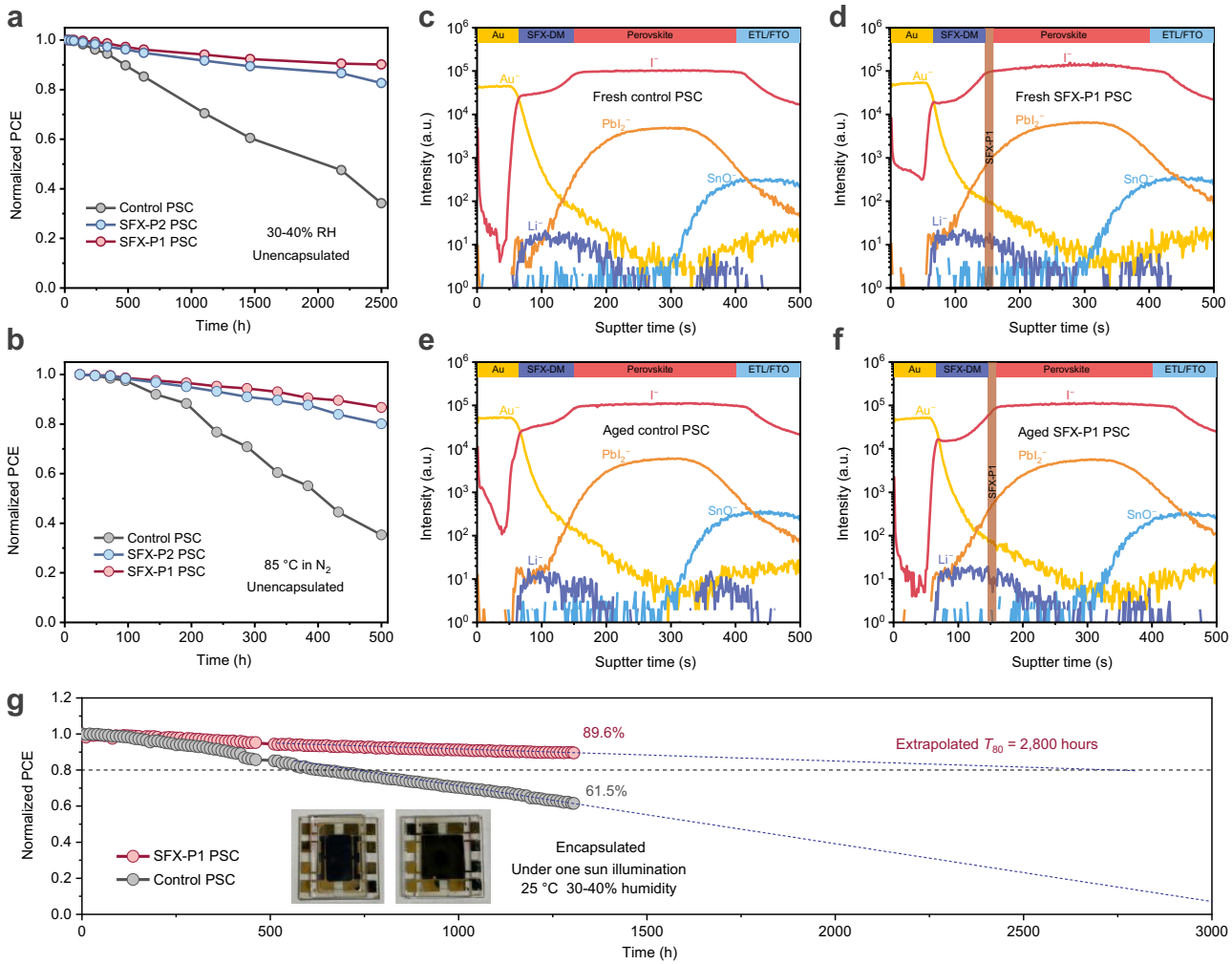

Fig. 5 | Stability of devices under various conditions. a Long-term moisture stability measurement of unencapsulated PSCs without and with SFX-P2 or SFX-P1 SAM modification, stored in ambient air with 30-40% humidity. **b** Thermal stability measurements of unencapsulated PSCs without and with SFX-P2 or SFX-P1 SAM modification at 85 °C in N_2 atmosphere. TOF-SIMS elemental depth profiles of **c** fresh control PSCs and **d** fresh SFX-P1-modified PSCs. TOF-SIMS elemental depth profiles of **e** control PSCs and **f** SFX-P1-modified PSCs after 100 hours of aging in the air (30-40% humidity) at 85 °C. **g** Operational stability measurements of encapsulated PSCs without and with SFX-P1 SAM modification under one-sun illumination in ambient air (30–40% humidity) with MPP tracking. Inset: photographs of the encapsulated devices.

perovskite surface modification and extends their applicability beyond specific device configurations, providing insights into the structural design of SAMs. In the future, tailoring SAM molecular structures and optimizing solvent processing are expected to play key roles in advancing perovskite photovoltaic technology.

Methods

Materials

Fluorine doped tin oxide (FTO) coated glass (TEC; 7 Ω sq^{-1}, Advanced Election Technology Co., Ltd.), formamidinium iodide (FAI; 99.90%, Advanced Election Technology Co., Ltd.), lead (II) iodide (PbI_2; 99.999%, Advanced Election Technology Co., Ltd.), Spiro-OMeTAD (99.86%, Advanced Election Technology Co., Ltd.), Nickel oxide nanoparticles (NiOx, 99.999%, Advanced Election Technology Co., Ltd.), Fullerene (C60, 99.5%, Advanced Election Technology Co., Ltd.), Bathocuproine (BCP, 99.5%, Advanced Election Technology Co., Ltd.), Hellmanex (special cleaning concentrate for cuvettes, Sigma Aldrich), isopropyl alcohol (IPA; 99.9%, TCI), ethyl ether (Et_2O; Sinopharm Chemical Reagent), chloroform (CF; Sinopharm Chemical Reagent), titanium diisopropoxide bis(acetylacetonate) (75% in TPA, TCI), ethanol (≥99.5%, Aladdin), tin (IV) oxide (SnO_2) colloid precursor (15% in H_2O colloidal dispersion, Alfa Aesar), polyacrylic acid (PAA, avg. MW = 450,000, Sigma Aldrich), 3-amino-1-propanesulfonic acid (SA; >98%, Sigma Aldrich), cesium iodide (CsI; >99%, TCI), methylammonium chloride (MACl; 99.5%, Xi'an Yuri Solar Co., Ltd.), li-bis(trifluoromethanesulfonyl)imide (Li-TFSI; 99%, Xi'an Yuri Solar Co., Ltd.), 4-*tert*-butylpyridine(*t*BP; 99%, Xi'an Yuri Solar Co., Ltd.), piperazine dihydriodide (PipDI, 99.5%, Xi'an Yuri Solar Co., Ltd.), *N*,*N*-dimethylformamide (DMF; 99.8%, Sigma-Aldrich), dimethyl sulfoxide (DMSO; 99.9%, Sigma-Aldrich), chlorobenzene (CB; 99.8%; Sigma-Aldrich), 2,7-dibromo-9*H*-fluoren-9-one (98%, Cat No.1137728, Leyan, Shanghai, China), sodium tert-butoxide (NaO^{t}Bu; 99%, Cat No.1253505, Leyan, Shanghai, China), tris(dibenzylideneacetone)dipalladium(0) ($Pd_2(dba)_3$; 98%, Cat No.1034548, Leyan, Shanghai, China), *p*-Toluenesulfonic acid monohydrate (98%, Cat No. 1037939, Leyan, Shanghai, China), potassium carbonate (99%, Cat No. 1715105, Leyan, Shanghai, China), tri-tert-butylphosphonium tetrafluoroborate ($P(^tBu)_2HBF_4$, 98%, Energy Chemicals), resorcinol (99%, Energy Chemicals), 1,2-dibromoethane (98%, Energy Chemicals), triethyl phosphite (98%, Energy Chemicals), bromoethane (99%, Energy Chemicals), bromotrimethylsilane (98%, Energy Chemicals). All chemical reagents were used as received without further purification unless otherwise specified.

Device fabrication

For fabricating *n-i-p* perovskite solar cells, the patterned FTO substrate was sequentially cleaned with Hellmanex (2%, deionized water), deionized water, acetone, and IPA in an ultrasonic bath, each for 20 min. The FTO substrate was then further cleaned using a UV-Ozone surface treatment for 15 minutes. A compact TiO_2 layer was deposited on top of the FTO glass using the spray pyrolysis method (O_2 as the carrier gas), and the substrate was preheated to 450 °C. A compact TiO_2 precursor solution was prepared by diluting 0.6 mL titanium diisopropoxide bis(acetylacetonate) (75 wt% in isopropanol) in 5.4 mL absolute ethanol. Note that the spraying process must be even and dense. After spray pyrolysis, the FTO/c-TiO_2 substrate was heated at 450 °C for 1 h and then cooled to ambient temperature. The thickness of c-TiO_2 is about 20 nm. The compact SnO_2 layer was fabricated by the PAA modification method. SnO_2 colloid precursor was diluted 25 times with deionized water and then mixed with PAA (1 mg mL^{-1}) under stirring at 80 °C for 2 h. The resulting solution was spin-coated onto the c-TiO_2 layer at 4000 rpm (2000 rpm s^{-1}) for 30 s. The substrates were heated at 160 °C for 30 min, followed by spin-coating 1 mg mL^{-1} SA solution at 3000 rpm (2000 rpm s^{-1}) for 30 s and annealing at 100 °C for 10 min. Before perovskite deposition, the FTO/TiO_2/SnO_2 substrate was treated with UV-Ozone for 15 min. The perovskite precursor solution comprising 20.2 mg MACl, 232.2 mg FAI, 39 mg CsI, 691.5 mg PbI_2, in 1 mL DMF-DMSO (4:1, *v*/*v*) was spin-coated in two steps, namely, 1000 rpm (500 rpm s^{-1}) for 5 s and 6,000 rpm (2000 rpm s^{-1}) for 45 s. With 20 s remaining, Et_2O (1 mL for FTO area of 15 mm × 15 mm) was quickly dispensed onto the middle of the substrate, and the films were annealed at 150 °C for 10 min in ambient conditions (relative humidity of 30-40%). The 60 µL of SFX-P1 or SFX-P2 dissolved in CB or CF (0.5, 1, 1.5, or 2 mg mL^{-1}) was dynamically spin-coated onto the perovskite film at 4000 rpm for 30 s, followed by annealing at 70 °C for 5 min. The HTM was deposited on the perovskite film by depositing a doped HTM solution at 4000 rpm for 25 s. The Spiro-OMeTAD solution (95 mg mL^{-1} in CB) doped with 39 µL *t*BP, 23 µL Li-TFSI (520 mg mL^{-1} in acetonitrile). The SFX-DM solutions (50 mg mL^{-1} in CB) were doped with 28 µL *t*BP, 17.5 µL Li-TFSI (520 mg mL^{-1} in acetonitrile). The Au electrode was thermally evaporated under high vacuum (<10^{-5} Pa) on top of the devices with the shadow mask. The thickness of the Au electrode was adjusted to 80 nm, and the evaporation speed was adjusted to 0.01 nm s^{-1} for the first 10 nm, 0.02 nm s^{-1} for the thickness between 10 nm and 20 nm, and 0.08 nm s^{-1} for the remaining 60 nm.

For fabricating *p-i-n* perovskite solar cells, the patterned ITO substrate was sequentially cleaned with Hellmanex (2%, deionized water), deionized water, acetone, and IPA in an ultrasonic bath, each for 20 min. The ITO substrate was then further cleaned by UV-Ozone surface treatment for 15 min. After that, NiO_x (10 mg mL^{-1} in H_2O: IPA = 3: 1) solution was spin-coated on the ITO substrate at 2000 rpm for 30 s and annealed in air at 120 °C for 20 min. The 60 µL of SFX-P1 or SFX-P2 dissolved in CF (1 mg mL^{-1}) was dynamically spin-coated onto the ITO/NiO_x substrate at 5000 rpm for 30 s, followed by annealing at 70 °C for 5 min. Afterwards, 100 µL of CF solution was dynamically spin-coated on ITO/NiO_x/SAM substrate to wash away the disordered molecular arrangement. The perovskite precursor solution comprising 245.04 mg FAI, 19.5 mg CsI, 691.5 mg PbI_2, in 1 mL DMF-DMSO (4:1, *v*/*v*) was spin-coated in two steps, namely, 2000 rpm (1000 rpm s^{-1}) for 10 s and 4000 rpm (2000 rpm s^{-1}) for 45 s. With 8 s remaining, CB (200 µL for ITO area of 25 mm x 25 mm) was quickly dispensed onto the middle of the substrate, and the films were annealed at 110 °C for 20 min in a N_2 glove box. Then, PipDI dissolved in IPA (0.3 mgmL^{-1} in IPA) solution was dynamically spin-coated on perovskite at 5000 rpm for 30 s and annealed at 110 °C for 5 min. C60 (25 nm), BCP (7 nm), and Ag (100 nm) were thermally evaporated under high vacuum (<10^{-5} Pa) onto the perovskite films with the shadow mask.

Computational details

The theoretical calculations were performed as follows. ESP mapping profile and ground-state orbital distribution of the Spiro-OMeTAD and SFX-based molecules were studied by performing B3LYP calculations with 6-31G (d,p) basis set in Gaussian 09 software package. Then, the Vienna Ab Initio Simulation Package (VASP) program was used to investigate the binding energy, assembly structures, and charge redistributions between the SFX-based molecules and $FAPbI_3$ perovskite. The generalized gradient approximation in the form of Perdew-Burke-Ernzerhof (GGA-PBE) was used for the exchange correlation function. All the geometry optimizations were performed with a cut-off energy of 400 eV and 3 × 3 × 1 *k*-point sampling. The convergence criteria for forces and energies were 0.05 eV Å^{-1} and 10^{-6} eV, respectively. The optimized SFX-based molecules were added to the target surfaces to simulate their adsorption geometry and energy on the $FAPbI_3$ perovskite (001) surfaces.

Characterization and measurements

The material characterizations were performed as follows. NMR spectra were recorded on an Agilent VNMRS 400 (or 600) MHz, and the chemical shifts were referenced internally using the residual solvent resonances. Matrix-assisted laser desorption ionization time of flight (MALDI-TOF) mass spectrum was acquired using an auto flex max Matrix-Assisted Laser Desorption/Ionization Time of Flight Mass Spectrometry. UV-vis absorption spectra were recorded using a Shimadzu UV-2450 spectrophotometer. CV was carried out on a CHI760E electrochemical workstation in dichloromethane containing tetrabutylammonium hexafluorophosphate (Bu_4NPF_6) (0.1 M) at a scan rate of 50 mV s^{-1} at room temperature under the protection of argon. The thermal decomposition temperatures of HTM were measured using TGA (Diamond TG/DTA) at a heating rate of 10 °C min^{-1} under nitrogen protection with a heating range of 30-600 °C. DSC (Discovery-DSC Q20) was performed under nitrogen flushing at a heating rate of 10 °C min^{-1} from 30 to 250 °C.

The film sample characterizations were performed as follows. The XPS and UPS were recorded by PHI5000 VersaProbe III. PYS (AC-2, Rikenkeiki) was performed to measure the ionization potential of thin films in air. SEM images were taken on a JEOL JSM-7800. AFM, C-AFM, and KPFM were recorded using a Cypher ES, Oxford Instruments, UK. AFM-IR for measuring the mapping of IR response was conducted on the ICONIR AFM-IR system (tapping mode, BRUKER) using an antimony-doped Si tip with reflective Au coating (spring constant: 42 N m^{-1}), the scanning size was 2×2 µm^2. GIWAXS images represented in the reciprocal lattice space were collected at the BL19B2 beamline at SPring-8 (Japan). The perovskite films were irradiated with an X-ray energy of 12.39 keV at a fixed-incident angle on the order of 0.12° and 2° through a Huber diffractometer. The 2D-GIWAXS images were recorded with a two-dimensional image detector (Pilatus 300 K). The PL and TRPL spectra were measured on a fluorescent spectrometer (FLS920). Confocal PL intensity maps were recorded with a laser confocal Raman spectrometer (Princeton Instruments, Acton Standard Series SP-2558) equipped with a 485 nm laser (PicoQuant LDH-P-C-485, 0.4 mW with a 1% optical density filter) using a home-built confocal microscope. Fs-TAS studies were performed on a home-made pump-probe system including a CMOS detector (S12198-1024Q, Hamamatsu) and the InGaAs photodiode array (G9203-256DA, Hamamatsu). The light source is generated by a Yb:KGW laser (Light conversion, Pharos, 1030 nm, 1 kHz repetition rate, 150 fs, 2 mJ per pulse), and the output laser was split into the pump beam and probe beam. The pump beam was used to generate the 515 nm excitation, and the probe beam was focused on a YAG plate to generate continuous white light. Water contact angles were measured using a JC2000D1 (manufacturer) contact angle instrument.

The device characterizations were performed as follows. TOF-SIMS (IONTOF system, PS02B11) was applied to detect the elemental

depth profiles in the PSC in a negative-ion mode. A Bi^+ primary beam (30 keV and 3 pA) and a Cs^+ sputter beam (1 keV and 75 nA) were used for ToF-SIMS measurement. The sputter size was 500 μm × 500 μm, and the analysis size was 100 μm × 100 μm for depth profiling. The light source for the *J-V* measurements comprises an AM 1.5 G solar simulator. The incident light intensity was 100 mW cm^{-2}, calibrated with a standard Si solar cell. The *J-V* curves were obtained by the linear sweep voltammetry (LSV) method using a Keithley 2400 source-measure unit. The measurement of the EQE was performed with a Newport QEPVSI-B photoelectric chemical quantum efficiency testing and analysis system. The active areas of the laboratory-test solar cells are 0.0625 cm^2 and 1 cm^2, and the aperture area for certification is 0.0434 cm^2.

Reporting summary

Further information on research design is available in the Nature Portfolio Reporting Summary linked to this article.

Data availability

The authors declare that the data supporting the findings of this study are available within the article and its Supplementary Information files. Additional details that support the findings of this study will be made available by the corresponding author upon request. Source data are provided with this paper.

References

1. Kojima, A., Teshima, K., Shirai, Y. & Miyasaka, T. Organometal halide perovskites as visible-light sensitizers for photovoltaic cells. *J. Am. Chem. Soc.* **131**, 6050–6051 (2009).
2. Yoo, J. J. et al. Efficient perovskite solar cells via improved carrier management. *Nature* **590**, 587–593 (2021).
3. Zhang, S. et al. Minimizing buried interfacial defects for efficient inverted perovskite solar cells. *Science* **380**, 404–409 (2023).
4. Chen, H. et al. Improved charge extraction in inverted perovskite solar cells with dual-site-binding ligands. *Science* **384**, 189–193 (2024).
5. Li, S. et al. High-efficiency and thermally stable FACsPbI3 perovskite photovoltaics. *Nature* **635**, 82–88 (2024).
6. Azmi, R. et al. Double-side 2D/3D heterojunctions for inverted perovskite solar cells. *Nature* **628**, 93–98 (2024).
7. Jiang, X. et al. Surface heterojunction based on n-type low-dimensional perovskite film for highly efficient perovskite tandem solar cells. *Natl. Sci. Rev.* **11**, nwae055 (2024).
8. Lin, R. et al. All-perovskite tandem solar cells with 3D/3D bilayer perovskite heterojunction. *Nature* **620**, 994–1000 (2023).
9. Suo, J. et al. Multifunctional sulfonium-based treatment for perovskite solar cells with less than 1% efficiency loss over 4500-h operational stability tests. *Nat. Energy* **9**, 172–183 (2024).
10. You, S. et al. Bifunctional hole-shuttle molecule for improved interfacial energy level alignment and defect passivation in perovskite solar cells. *Nat. Energy* **8**, 515–525 (2023).
11. Xiao, Y., Yang, X., Zhu, R. & Snaith, H. J. Unlocking interfaces in photovoltaics. *Science* **384**, 846–848 (2024).
12. Li, B. et al. Fundamental understanding of stability for halide perovskite photovoltaics: The importance of interfaces. *Chem* **10**, 35–47 (2024).
13. Jiang, Q. et al. Surface passivation of perovskite film for efficient solar cells. *Nat. Photonics* **13**, 460–466 (2019).
14. Xu, C. et al. Molecular ferroelectric self-assembled interlayer for efficient perovskite solar cells. *Nat. Commun.* **16**, 835 (2025).
15. Wang, J. et al. Dipolar Carbazole ammonium for broadened electric field distribution in high-performance perovskite solar cells. *J. Am. Chem. Soc.* **147**, 8663–8671 (2025).
16. Kim, G. M., Sato, H., Ohkura, Y., Ishii, A. & Miyasaka, T. Phenethylamine-based interfacial dipole engineering for high voc triple-cation perovskite solar cells. *Adv. Energy Mater.* **12**, 2102856 (2022).
17. Wang, H. et al. Interface Dipole Management of D-A-Type Molecules for Efficient Perovskite Solar Cells. *Angew. Chem. Int Ed.* **63**, e202404289 (2024).
18. Zang, X. et al. Passivating Dipole Layer Bridged 3D/2D Perovskite Heterojunction for Highly Efficient and Stable p-i-n Solar Cells. *Adv. Mater.* **36**, 2309991 (2024).
19. Shi, J. et al. Dual-Site molecular dipole enables tunable interfacial field toward efficient and stable perovskite solar cells. *Adv. Mater.* **36**, 2410464 (2024).
20. Wang, D. et al. Tailoring Interfacial Dipole Molecules to Mitigate Carrier and Energy Losses in Perovskite Solar Cells. *Adv. Funct. Mater.* **35**, 2412068 (2024).
21. Yang, T., Zhao, W., Liu, X. & Liu, S. Tailoring the Interfacial Termination via Dipole Interlayer for High-Efficiency Perovskite Solar Cells. *Adv. Energy Mater.* **13**, 2204192 (2023).
22. Chen, Q., Wang, C., Li, Y. & Chen, L. Interfacial Dipole in Organic and Perovskite Solar Cells. *J. Am. Chem. Soc.* **142**, 18281–18292 (2020).
23. Isikgor, F. H. et al. Molecular engineering of contact interfaces for high-performance perovskite solar cells. *Nat. Rev. Mater.* **8**, 89–108 (2022).
24. Azmi, R. et al. High-efficiency low-temperature ZnO based perovskite solar cells based on highly polar, nonwetting self-assembled molecular layers. *Adv. Energy Mater.* **8**, 1701683 (2018).
25. Wojciechowski, K. et al. Heterojunction modification for highly efficient organic–inorganic perovskite solar cells. *ACS Nano* **8**, 12701–12709 (2014).
26. Zuo, L. et al. Enhanced photovoltaic performance of CH3NH3PbI3 perovskite solar cells through interfacial engineering using self-assembling monolayer. *J. Am. Chem. Soc.* **137**, 2674–2679 (2015).
27. Magomedov, A. et al. Self-assembled hole transporting monolayer for highly efficient perovskite solar cells. *Adv. Energy Mater.* **8**, 1801892 (2018).
28. Shou, K. et al. Ultralow surface energy self-assembled monolayers of iodo-perfluorinated alkanes on silica driven by halogen bonding. *Nanoscale* **11**, 2401–2411 (2019).
29. Al-Ashouri, A. et al. Monolithic perovskite/silicon tandem solar cell with >29% efficiency by enhanced hole extraction. *Science* **370**, 1300–1309 (2020).
30. Suo, J., Yang, B., Bogachuk, D., Boschloo, G. & Hagfeldt, A. The dual use of SAM molecules for efficient and stable perovskite solar cells. *Adv. Energy Mater.* **15**, 2400205 (2025).
31. Levine, I. et al. Charge transfer rates and electron trapping at buried interfaces of perovskite solar cells. *Joule* **5**, 2915–2933 (2021).
32. Al-Ashouri, A. et al. Conformal monolayer contacts with lossless interfaces for perovskite single junction and monolithic tandem solar cells. *Energy Environ. Sci.* **12**, 3356–3369 (2019).
33. Li, W. et al. A homonuclear molecule with a permanent electric dipole moment. *Science* **334**, 1110–1114 (2011).
34. Xiao, B. et al. Energy level alignment regulation and carrier management in perovskite solar cells with various bandgaps using tailored metal-organic frameworks. *Adv. Funct. Mater.* **35**, 2417293 (2025).
35. Campbell, I. H. et al. Controlling charge injection in organic electronic devices using self-assembled monolayers. *Appl Phys. Lett.* **71**, 3528–3530 (1997).
36. Zhao, K. et al. Peri-Fused polyaromatic molecular contacts for perovskite solar cells. *Nature* **632**, 301–306 (2024).
37. Peng, Y. et al. Enlarging moment and regulating orientation of buried interfacial dipole for efficient inverted perovskite solar cells. *Nat. Commun.* **16**, 1252 (2025).

38. Zhu, J. et al. A donor–acceptor-type hole-selective contact reducing non-radiative recombination losses in both subcells towards efficient all-perovskite tandems. *Nat. Energy* **8**, 714–724 (2023).
39. Tan, Q. et al. Inverted perovskite solar cells using dimethylacridine-based dopants. *Nature* **620**, 545–551 (2023).
40. Zheng, X. et al. Co-deposition of hole-selective contact and absorber for improving the processability of perovskite solar cells. *Nat. Energy* **8**, 462–472 (2023).
41. Wang, F. et al. A polymeric hole transporter with dual-interfacial interactions enables 25%-efficiency blade-coated perovskite solar cells. *Adv. Mater.* **36**, 2412059 (2024).
42. Truong, M. A. et al. Molecular Design of Hole-Collecting Materials for Co-Deposition Processed Perovskite Solar Cells: A Tripodal Triazatruxene Derivative with Carboxylic Acid Groups. *J. Am. Chem. Soc.* **147**, 2797–2808 (2025).
43. Sadhu, S. et al. Unexpected surface interactions between fluorocarbons and hybrid organic inorganic perovskites evidenced by PM-IRRAS and their application towards tuning the surface potential. *Mater. Horiz.* **6**, 192–197 (2019).
44. Canil, L. et al. Tuning halide perovskite energy levels. *Energy Environ. Sci.* **14**, 1429–1438 (2021).
45. Jiang, X. et al. Molecular Dipole Engineering of Carbonyl Additives for Efficient and Stable Perovskite Solar Cells. *Angew. Chem. Int Ed.* **62**, e202302462 (2023).
46. Zhang, X. et al. A spiro-type self-assembled hole transporting monolayer for highly efficient and stable inverted perovskite solar cells and modules. *Energy Environ. Sci.* **18**, 468–477 (2025).
47. Zhai, M. et al. Fluorene-Terminated π-Conjugated Spiro-Type Hole Transport Materials for Perovskite Solar Cells. *ACS Energy Lett.* **10**, 915–924 (2025).
48. Wu, T. et al. Lattice Matching Anchoring of Hole-Selective Molecule on Halide Perovskite Surfaces for n-i-p Solar Cells. *Adv. Mater.* **37**, e2414576 (2025).
49. Wang, A. et al. Halogenated Hole Selective Contact Enhances Interfacial Weak Bonding of Perovskite Solar Cells. *Adv. Energy Mater.* **14**, 2400640 (2024).
50. Zhai, M. et al. Construction of Efficient $Cs_2AgBiBr_6$ perovskite solar cells by enhancing hole-selective contact with deep-level dopant-free hole transport material. *Adv. Funct. Mater.* **34**, 2315428 (2024).
51. Luo, X. et al. Effect of solution-state aggregation on solid-state crystal orientation in donor–acceptor conjugated copolymers. *Chem. Mater.* **36**, 3726–3734 (2024).
52. Jiang, K., Wu, F., Zhang, G., Zhu, L. & Yan, H. Efficient Perovskite Solar Cells Based on Dopant-Free Spiro-OMeTAD Processed With Halogen-Free Green Solvent. *Sol. RRL* **3**, 1900061 (2019).
53. Zhai, M. D. et al. Perovskite solar cells and modules employing facile synthesis and green-solvent-processable organic hole transport materials. *ACS Energy Lett.* **8**, 4966–4975 (2023).
54. Shibayama, N. et al. Control of molecular orientation of spiro-OMeTAD on substrates. *ACS Appl Mater. Interfaces* **12**, 50187–50191 (2020).
55. Deng, X. et al. Co-assembled monolayers as hole-selective contact for high-performance inverted perovskite solar cells with optimized recombination loss and long-term stability. *Angew. Chem. Int Ed.* **61**, e202203088 (2022).
56. Zheng, X. et al. Suppressing phase segregation and nonradiative losses by a multifunctional cross-linker for high-performance all-perovskite tandem solar cells. *Energy Environ. Sci.* **18**, 2995–3004 (2025).
57. Hu, X. et al. Multi-Functional Spirobifluorene Phosphonate Based Exciplex Interface Enables Voc Reaching 95% of Theoretical Limit for Perovskite Solar Cells. *Adv. Mater.* **36**, 2313099 (2024).
58. Li, C., Zhang, N. & Gao, P. Lessons learned: how to report XPS data incorrectly about lead-halide perovskites. *Mater. Chem. Front.* **7**, 3797–3802 (2023).
59. Yang, B., Cai, B., Zhou, T., Zheng, X. & Zhang, W.-H. Facile and sustainable interface modulation via a self-assembly phosphonate molecule for efficient and stable perovskite photovoltaics. *Chem. Eng. J.* **488**, 150861 (2024).
60. Yang, S. et al. Stabilizing halide perovskite surfaces for solar cell operation with wide-bandgap lead oxysalts. *Science* **365**, 473–478 (2019).
61. Wen, H. et al. Synergistic full-scale defect passivation enables high-efficiency and stable perovskite solar cells. *Adv. Energy Mater.* **13**, 2301813 (2023).
62. Vanin F. et al. Modulating perovskite surface energetics through tuneable ferrocene interlayers for high-performance perovskite solar cells. *Angew Chem. Int. Ed.*, e202424041 (2025).
63. Wang, B. et al. Robust molecular dipole-enabled defect passivation and control of energy-level alignment for high-efficiency perovskite solar cells. *Angew. Chem. Int Ed.* **60**, 17664–17670 (2021).
64. Cao, Y. et al. Interface modification by ammonium sulfamate for high-efficiency and stable perovskite solar cells. *Adv. Energy Mater.* **13**, 2302103 (2023).
65. Liu, X. et al. Extending the pi-conjugated system in spiro-type hole transport material enhances the efficiency and stability of perovskite solar modules. *Angew. Chem. Int Ed.* **62**, e202304350 (2023).
66. Wang, L., McCleese, C., Kovalsky, A., Zhao, Y. & Burda, C. Femtosecond Time-Resolved Transient Absorption Spectroscopy of CH3NH3PbI3 Perovskite Films: Evidence for Passivation Effect of PbI2. *J. Am. Chem. Soc.* **136**, 12205–12208 (2014).
67. Shen, Y., Deng, K., Chen, Q., Gao, G. & Li, L. Crowning lithium ions in hole-transport layer toward stable perovskite solar cells. *Adv. Mater.* **34**, e2200978 (2022).
68. Bao, H., Liu, H., Wang, S., Ma, J. & Li, X. Restricting lithium-ion migration via Lewis base groups in hole transporting materials for efficient and stable perovskite solar cells. *Chem. Eng. J.* **433**, 133534 (2022).
69. Kim, S.-G. et al. Capturing mobile lithium ions in a molecular hole transporter enhances the thermal stability of perovskite solar cells. *Adv. Mater.* **33**, 2007431 (2021).

Acknowledgements

This work was financially supported by the National Natural Science Foundation of China (22179053 by M. C., 22279046 by C. C.), Natural Science Excellent Youth Foundation of Jiangsu Province (BK20220112 by M. C.), Special Foundation for Carbon Peak Carbon Neutralization Technology Innovation Program of Jiangsu Province (BE2022026-2 by M. C.), JSPS KAKENHI (24H00486 by T. M.). The GIWAXS measurements were performed at SPring-8 with the approval of the JASRI (2024A1902 and 2024B1697 by N. S.). The authors acknowledge the Tokuo Fujii Research Fund for Support of the Article Processing Charge of International Academic Papers. The authors extend their gratitude to Mr. Shijun Chou (from Scientific Compass www.shiyanjia.com) for providing invaluable assistance with the UPS analysis. The authors would like to thank Mr. Weihao Xing from SCl-GO (www.sci-go.com) for the NMR analysis. The SEM measurements were supported by Beijing Zhongkebaice Technology Service Co., Ltd. (www.zkbaice.cn). The authors thank the Analysis Center of Fukuoka Industry-Academia Symphonicity for characterizations by using AFM-IR.

Author contributions

M.Z. conceived the idea, synthesized, and characterized molecules. M.Z. and K.D. fabricated devices and prepared samples for characterization. T.W., J.S., and A.S. performed theoretical calculations. K.D., A.W., and T.M. characterized the samples with TRPL, UPS, SEM, DSC, TPC, and TPV measurements. N.S. performed GIWAXS characterization. K.N. and J.Song conducted TOF-SIMS characterization. A.K., Y.W., and S.Z. constructed DD device simulations and conducted data analysis. P.W., S.I.,

K.T., S.Y., and Z.G. conducted the AFM, KPFM, and AFM-IR measurements. M.Z. wrote the initial draft, and C.C., Z.G., T.M., and M.C. revised the manuscript. Z.G., T.M., and M.C. supervised this project. All authors discussed the results and contributed to the revisions of the manuscript.

Competing interests
The authors declare no competing interests.

Additional information
Supplementary information The online version contains supplementary material available at https://doi.org/10.1038/s41467-026-69198-2.

Correspondence and requests for materials should be addressed to Zhanglin Guo, Toshinori Matsushima or Ming Cheng.

Peer review information *Nature Communications* thanks Emilio Palomares and the other anonymous reviewer(s) for their contribution to the peer review of this work. A peer review file is available.